Journal of
Ceramic Science
and Technology

J. Ceram. Sci. Technol., **09** [3] 345-352 (2018)
DOI: 10.4416/JCST2018-00018
available online at: http://www.ceramic-science.com
© 2018 Göller Verlag

Short Communication

Co-Precipitation Synthesis of $La_2O_2SO_4:Tb^{3+}$ Phosphor and its Conversion to $La_2O_2S:Tb^{3+}$ Ceramic Scintillator *via* Pressureless Sintering in Hydrogen

G.X. Xu, J.B. Lian*, N.C. Wu, X. Zhang, J. He

School of Mechanical Engineering, New Functional Materials Laboratory,
Liaoning Shihua University, Fushun, 113001, P.R. China

received March 1, 2018; received in revised form April 6, 2018; accepted April 23, 2018

Abstract

This research reports on the synthesis of a series of lanthanum compounds. As an intermediate product, $La_2O_2SO_4:Tb^{3+}$phosphors were prepared with a co-precipitation method. $La_2O_2S:Tb^{3+}$ ceramic scintillator was then synthesized by means of pressureless reaction sintering in a hydrogen atmosphere. XRD patterns show that the crystal structure of the precursor is unidentified, and it can be transformed into pure $La_2O_2SO_4$ phase after calcination at 800 °C in air. Compared with the Tb^{3+}-ions-doped precursor, the $La_2O_2SO_4:Tb^{3+}$ phosphor has a stronger green emission peak at around 542 nm, which is attributed to $^5D_4 \rightarrow {}^7F_5$ transition of Tb^{3+} ions. The $La_2O_2SO_4:Tb^{3+}$ phosphor exhibits the highest green luminescence when the concentration of Tb^{3+} is 12 %. The corresponding decay process ($^5D_4 \rightarrow {}^7F_4$) of the $La_2O_2SO_4$:12%Tb^{3+} phosphor can be fitted into a double exponential function with 0.217 μs and 2.212 μs for t_1 and t_2, respectively. $La_2O_2S:Tb^{3+}$ ceramic scintillator could be fabricated by sintering the $La_2O_2SO_4:Tb^{3+}$ phosphor in a hydrogen atmosphere. It appears greenish yellow with good translucency and light output performance.

Keywords: Lanthanum compounds, co-precipitation, pressureless sintering, photoluminescence, ceramic scintillator

I. Introduction

Lanthanides (Ln) compounds, as one part of rare earth (RE) materials, include numerous host matrixes, such as oxysulfates [1], oxysulfides [2], phosphates [3,4], molybdates [5], sulfides [6] and fluorides [7]. Ln oxysulfates ($Ln_2O_2SO_4$) have attracted considerable interest from researchers because of their low toxicity, unique luminescence behavior and sharp emission peaks [8,9]. Accordingly, they have been widely applied in bioimaging and photochemical reactions [10], optical temperature sensors [11] and so on. $Ln_2O_2SO_4$ powder is conventionally synthesized with the molten salt method [12], thermal decomposition synthesis [13], the homogeneous precipitation method [14], the surfactant-assisted technique [15] and hydrothermal synthesis [16]. However, the procedures involved in these routes are complicated, and it is generally difficult to get the resulting products with good morphology. It is worth noting that the luminescent efficiency of $Ln_2O_2SO_4:RE^{3+}$ phosphors greatly depends on size, shape, morphology and dispersibility, etc. Therefore, it is necessary to prepare the $Ln_2O_2SO_4:RE^{3+}$ phosphors with excellent properties with a suitable method. The co-precipitation method has been widely used [17]. Not only does it provide a good way to obtain a tunable size and good morphology, it can also greatly reduce costs as it involves an easy-to-control process. To the best of our knowledge, $Ln_2O_2SO_4$ can convert into Ln oxysulfide (Ln_2O_2S) under reduction conditions [18]. Compared with $Ln_2O_2SO_4$, Ln_2O_2S exhibits low symmetry, a wide band-gap (4.6–4.8 eV), high light absorption and excellent chemical stability [19–21], and it is considered an excellent luminescent host. Since La^{3+} ions have no *4f* electrons, possessing a closed shell and optically inert properties, La_2O_2S has been explored extensively in fluorescence applications for many years [22–24].

To date, many glass scintillator and single crystal materials have been put into practical application in medical imaging devices. However, some of them have an amorphous structure with poor cleavage properties and difficult-to-obtain high surface quality, resulting in the limitation of their application range [25]. In comparison, ceramic scintillators are regarded as a new generation in detection materials owing to uniform doping concentration on molecular level, average grain size, high scintillation efficiency, low cost, etc., and have found numerous uses in X-ray detectors, intensifying screens and charge-coupled devices (CCD) [26,27]. Researchers have focused on preparation of RE^{3+}-ions-doped La_2O_2S ceramic scintillators. Yu.V. Orlovskii *et al.* has fabricated Nd^{3+}-doped La_2O_2S ceramic with the hot pressing sintering method and obtained good properties [28]. Later, our group firstly tried to prepare $La_2O_2S:Eu^{3+}$ ceramic by means of pressureless reaction sintering with $La_2O_2SO_4:Eu^{3+}$ nanoparticle as the intermediate product [18], which simplifies the process

* Corresponding author: lianjingbao@aliyun.com

while reducing the cost. No paper seems to have touched upon Tb^{3+}-ions-doped La_2O_2S ceramic scintillator.

In this article, $La_2O_2SO_4$:Tb^{3+} phosphor was synthesized with a co-precipitation method and then the corresponding La_2O_2S:Tb^{3+} ceramic scintillator was fabricated by means of pressureless reaction sintering in hydrogen. The comparison of phase, photoluminescence between the Tb^{3+}-ions-doped precursor and $La_2O_2SO_4$:Tb^{3+} phosphors is discussed in detail. Furthermore, the scintillation properties of La_2O_2S:Tb^{3+} ceramic scintillator have also been investigated.

II. Experimental Procedure

(1) Sample preparation

$La_2O_2SO_4$ was synthesized with the co-precipitation method. The starting materials for synthesis were La_2O_3 (99.99 % purity), Tb_4O_7 (99.99 % purity), HNO_3 (AR), NH_3H_2O (AR) and $(NH_4)_2SO_4$ (AR). According to the host lattice of La_2O_2S, the Tb^{3+} ions (primary activator) concentration was set in the range of 0 – 18 mol% and filled with the decrease of La^{3+} ions. Firstly, 0.1 M $(La_{1-x},Tb_x)_2(NO_3)_3$ solution was prepared by dissolving La_2O_3 and Tb_4O_7 into diluted nitric acid. Then, $(NH_4)_2SO_4$ was added in the molar ratio of 2:1.5 for $[La^{3+}+Tb^{3+}]$:SO_4^{2-} to form the mother liquor. A 3M $NH_3 \cdot H_2O$ solution was prepared as precipitant agent by diluting ammonia water in deionized water. The precursors were then obtained by dropping 3M $NH_3 \cdot H_2O$ into the mother liquor at 2 $mL \cdot min^{-1}$ under constant stirring. In the synthesis process, in order to keep the pH value at 9, the ZD-2A automatic potential titrator was used to monitor the reaction system. After dropping, the precipitate was allowed to set for 2 h, then washed and separated with deionized water and alcohol to obtain the precursors. The obtained precursors were heated at 80 °C for half a day, followed by calcining at 800 °C for 2 h in air. The products were pressed into disks under 200 MPa pressure by means of uniaxial compaction. Finally, the prepared phosphors were sintered at 1500 °C in a hydrogen atmosphere for 2 h and cooled down to room temperature in a tubular furnace to obtain the La_2O_2S:Tb^{3+} ceramic scintillator.

(2) Sample characterization

The structure and phase purity were investigated with X-ray powder diffraction tools with CuKα = 1.5406 Å. A TU1901 spectrometer with barium sulfate as a reference was adapted to record the absorption spectra. Photoluminescence (PL) spectra and decay time were analyzed with a Hitachi F-7000 fluorescence spectrophotometer equipped with IBH TemPro fluorescence lifetime measurement system. The luminous photographs were obtained on a Boteng Ultraviolet Light Analyzer with the light power density of 0.8 $mW \cdot mm^{-2}$. The 1931 CIE standard for colorimetry was used to calculate CIE coordinates. The light intensity output was measured with a charge-coupled device (90 kV, 2 mA), a commercial $CdWO_4$ single crystal being used as a reference.

III. Results and Discussion

(1) Phase structure analyses

To aid understanding of the phase structure of the samples, the XRD patterns of the precursor, the corresponding calcination product as well as the standard JCPDS card of $La_2O_2SO_4$ are shown in Fig. 1. As can be seen from Fig. 1(a), the diffraction peaks are well-defined, indicating the crystal structures of the precursor are better in nature. However, the obtained diffraction pattern is inconsistent with the data reported in the JCPD card database and the crystal structure is yet to be identified. After calcination at 800 °C for 2 h in air, the diffraction peaks of the obtained sample are well indexed to the tetragonal phase of $La_2O_2SO_4$ (JCPDS no.00 – 016 – 0501) without any impurity peaks, as shown in Fig. 1(b). It suggests that the precursor can be completely transformed into $La_2O_2SO_4$. In addition, the characteristic peaks of $La_2O_2SO_4$ phase are sharper and stronger, indicating that the grain size and crystallization have increased to some extent.

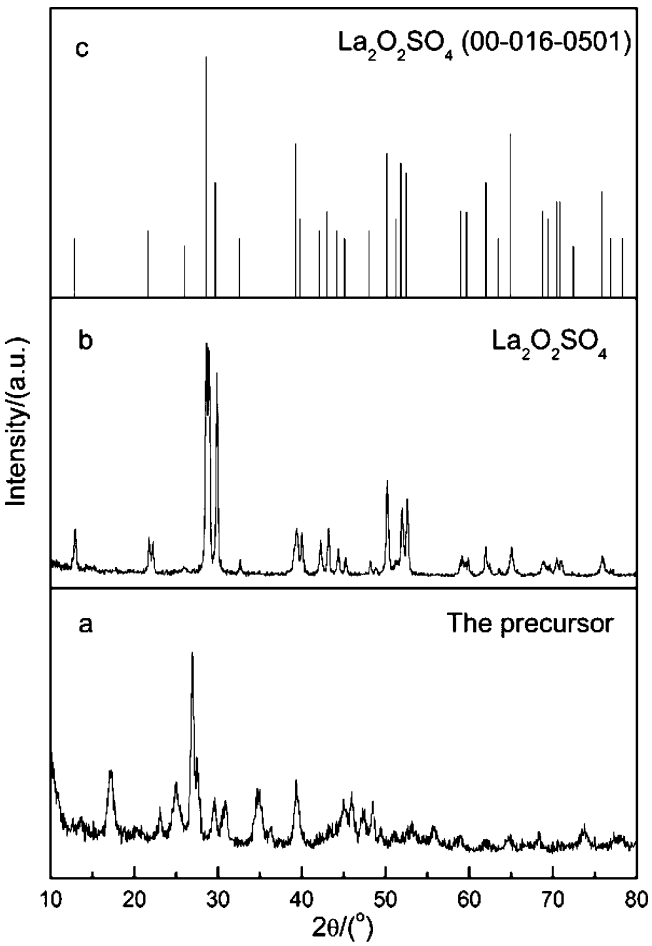

Fig. 1: XRD patterns of (a) the precursor; (b) $La_2O_2SO_4$ nanoparticle and (c) JCPDS card of $La_2O_2SO_4$.

(2) Photoluminescence properties

Fig. 2 shows the PL excitation (Fig. 2(a)) and emission spectra (Fig. 2(b)) of the Tb^{3+}-ions-doped precursor and $La_2O_2SO_4$:Tb^{3+} phosphor, respectively. According to the excitation spectra (Fig. 2(a)) monitored at 542 nm, a dominant peak at around 374 nm is shown, assigned to the

$^7F_6 \rightarrow {}^5D_3$ transition of Tb^{3+} ions. The characteristic peak at around 230 nm is attributed to $4f^8 \rightarrow 4f^75d^1$ transition of Tb^{3+} ions. Weak peaks at around 317 nm, 350 nm and 484 nm can be ascribed to $^8S_{7/2} \rightarrow {}^6I_{11/2}$ transition of La^{3+} ions, $^7F_6 \rightarrow {}^5D_2$ and $^7F_6 \rightarrow {}^5D_4$ transition of Tb^{3+} ions, respectively. At around 215 nm, the $La_2O_2SO_4:Tb^{3+}$ phosphor shows a narrow characteristic peak while it does not appear in the precursor, this may be related to the band gap self-absorption of the $La_2O_2SO_4$ host lattice (E_g =5.2 eV). Fig. 2(b) shows the emission spectra on excitation at 374 nm. It consists of four emission peaks at around 623 nm, 590 nm, 542 nm and 487 nm, arising from the $^5D_4 \rightarrow {}^7F_J$ (J = 3, 4, 5 and 6) transitions of Tb^{3+} ions, respectively. The peak near at 542 nm exhibits the strongest green emission. On the whole, the two samples have a similar variation trend, but the peak intensity of the precursor is far less than that of the $La_2O_2SO_4:Tb^{3+}$phosphor. The reason might be the reduction of organic residues (OH^- and CO_3^{2-}) as well as the better crystallization and small grain size after calcination [29]. Besides, the effects of surface roughness on internal reflection might be another factor that cannot be ignored [30].

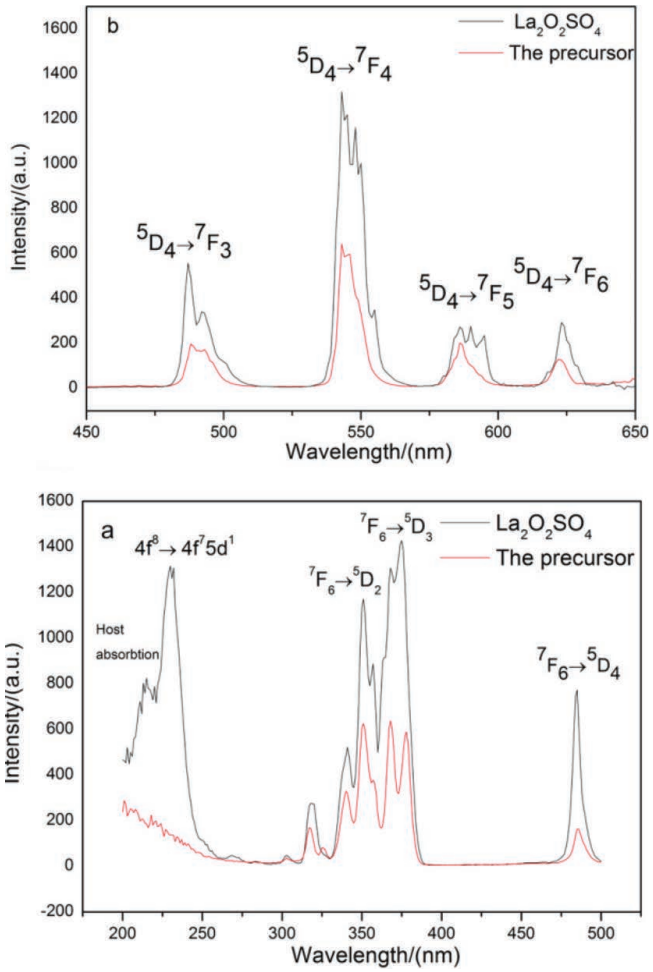

Fig. 2: Photoluminescence excitation (a) and emission spectra (b) of the Tb^{3+}-ions-doped precursor (black) and $La_2O_2SO_4$ nanoparticle (red).

To gain more insight into the energy transfer mechanism of the $La_2O_2SO_4:Tb^{3+}$ phosphor, the energy level diagram is shown in Fig. 3. Firstly, electrons at ground state were excited to excited state because of the absorption of $La_2O_2SO_4$ host, then the excitation energy was transferred to the Tb^{3+} ions, which was probably caused by the diffusion of free e^- and h^+ and their capture at the Tb^{3+} ions site. When the Tb^{3+} ions accepted the excitation energy, the electrons transformed from the ground state $^4F_6$ to excited state $^4F_7{}^5D_1$. Finally, electrons radiatively relaxed to ground state, leading to the transition of $^5D_{3,4} \rightarrow {}^7F_J$ (J = 3, 4, 5, 6) and a green emission.

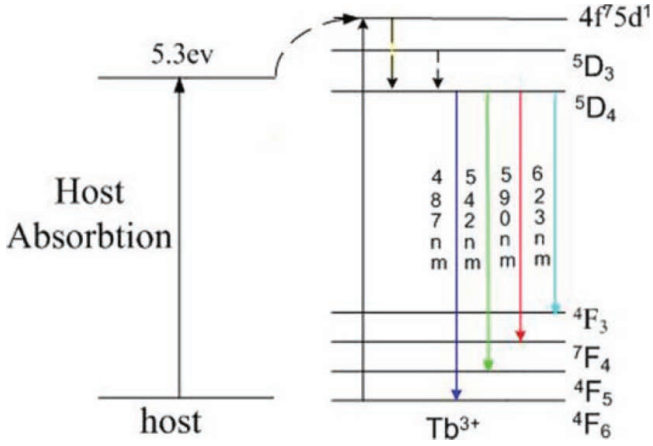

Fig. 3: Energy level diagram of energy transformation in a $La_2O_2SO_4:Tb^{3+}$ nanoparticle.

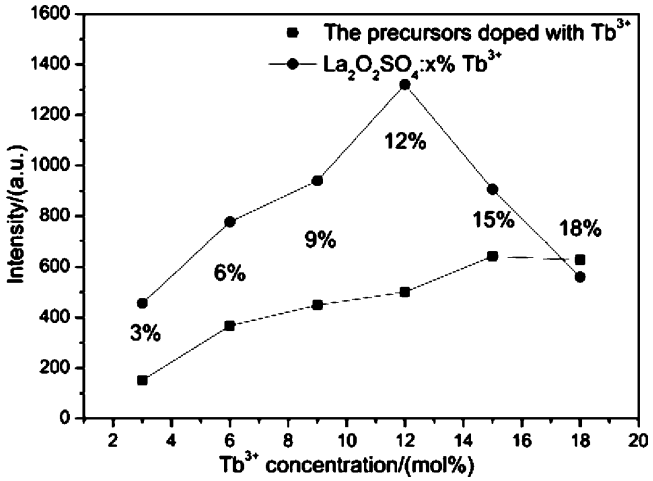

Fig. 4: Relationship between Tb^{3+} ions doping concentration and luminescent intensity of the precursor and a $La_2O_2SO_4$ nanoparticle.

Fig. 4 shows the relationship curves between the emission intensity of the $^5D_4 \rightarrow {}^7F_5$ transition and the Tb^{3+} ions concentration. It reveals that as the concentration of Tb^{3+} ions increases, the emission intensity increases accordingly. Once the Tb^{3+} ions reach maximum concentration, the emission intensity decreases quickly, which can arise from the concentration quenching. Note that the maximum concentration of precursor (x = 15 %) is higher than that of the $La_2O_2SO_4:x\%Tb^{3+}$ phosphor (x = 12 %) under the same excitation. It may be that large numbers of boundary confinements exist in the precursor compared to in the $La_2O_2SO_4$, which greatly hinders the energy transfer from doping ions to defect states [31].

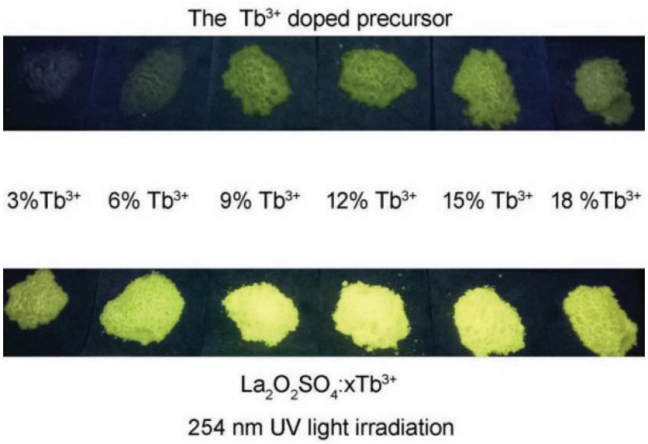

Fig. 5: The luminescent photos of x%Tb^{3+}-ions-doped precursor and $La_2O_2SO_4$ nanoparticle (x = 3 %, 6 %, 9 %,12 % 15 % and 18 %).

Fig. 5 shows the luminescence photos of the Tb^{3+}-ions-doped precursors and $La_2O_2SO_4$:*x*%Tb^{3+} phosphors under 254 nm UV light irradiation. It can be seen that as concentration of the Tb^{3+} ions concentration increases, the two samples appear greenish-yellow to the naked eye, and the brightness trends are in agreement with Fig. 4. In order to study the effects of doping concentration on color composition further, the CIE chromaticity diagrams of the Tb^{3+}-ions-doped precursors and $La_2O_2SO_4$:*x*%Tb^{3+} phosphors are shown in Fig. 6. It can be seen that all the coordinates are located in the green light area. The coordinates of the precursor doped with *x*%Tb^{3+} ions (*x* = 3 %, 6 %, 9 %, 12 %, 15 % and 18 %) are (0.3535, 0.5005), (0.3514, 0.5349), (0.3527, 0.5454), (0.3534, 0.5478), (0.3530, 0.5559) and (0.3535, 0.5553), respectively. The coordinates of $La_2O_2SO_4$:*x*%Tb^{3+} (*x*=3%, 6%, 9%, 12%, 15% and 18%) phosphors are (0.3505, 0.5513), (0.3365, 0.5746), (0.3374, 0.5745), (0.3403, 0.5756), (0.3481, 0.5719) and (0.3496, 0.5681), respectively. Moreover, the purest green emission dot coordinates of the precursor doped with Tb^{3+} ions and $La_2O_2SO_4$:Tb^{3+} phosphor are (0.3530, 0.5559) and (0.3403, 0.5756), corresponding to the concentration of 15 % and 12 %, respectively, which is in accordance with the luminescent photos of the Tb^{3+}-ions-doped precursor and $La_2O_2SO_4$:Tb^{3+} phosphor and concentration quench curves.

Fig. 7 shows the decay curves of the 15%Tb^{3+}-ions-doped precursor and $La_2O_2SO_4$:12%Tb^{3+} phosphor, monitored based on $^5D_4 \rightarrow {}^7F_4$ transition of Tb^{3+} ions under 374 nm UV irradiation. It shows that the decay curves are fitted into a double exponential function: $I(t)=I_0+A_1\exp(-t/\tau_1)+A_2\exp(-t/\tau_2)$, where I(t), I_0 and τ represent the luminescence intensity, initial intensity and decay time, respectively. The lifetime of the 15%Tb^{3+}-ions-doped precursor and $La_2O_2SO_4$:12%Tb^{3+} phosphor are 0.090 ms, 0.740 ms and 0.217 ms, 2.212 ms, respectively. It is clear that $La_2O_2SO_4$:12%Tb^{3+} phosphor possesses a longer lifetime and the main reason is consistent with the PL spectra.

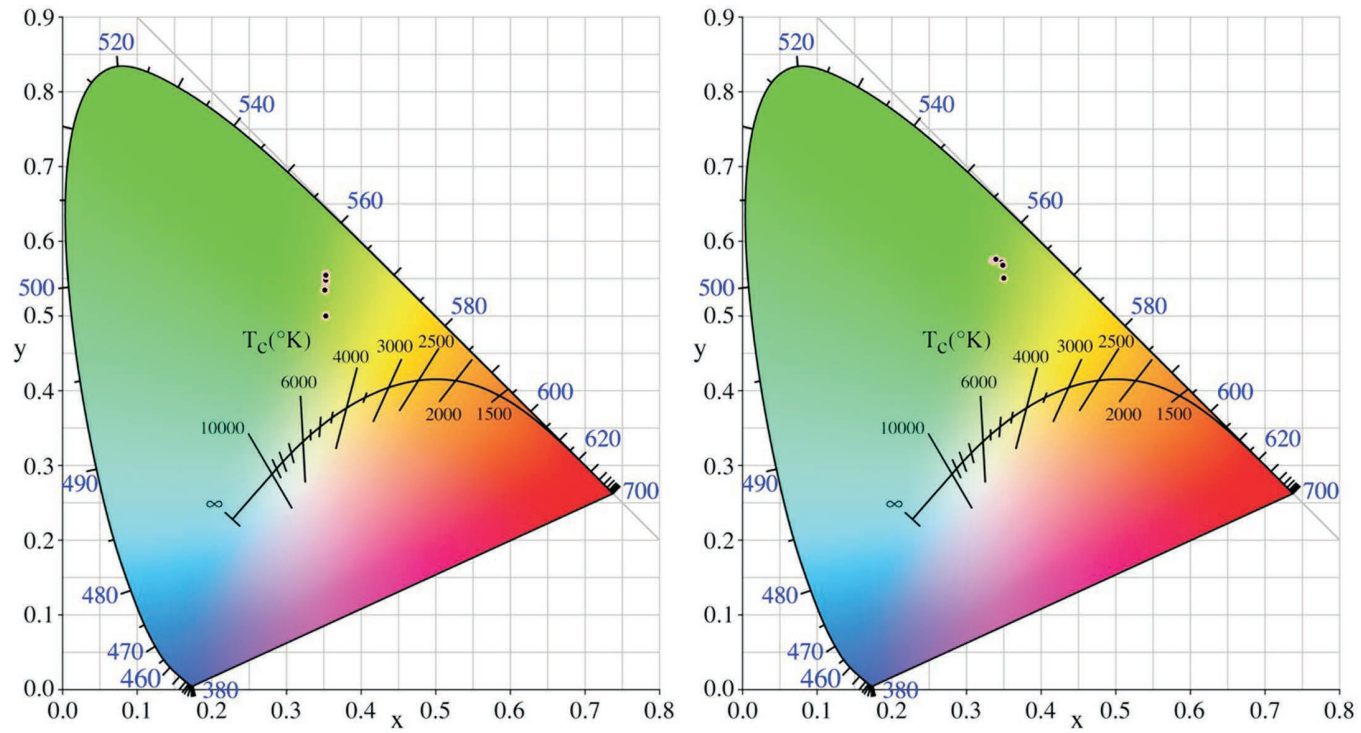

Fig. 6: CIE chromaticity diagrams of Tb^{3+}-ions-doped precursor (left) and $La_2O_2SO_4$ nanoparticle (right).

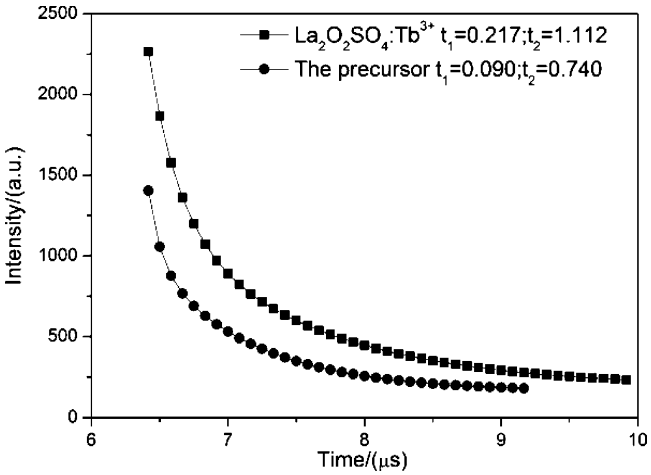

Fig. 7: Decay curves of Tb^{3+}-ions-doped precursor and $La_2O_2SO_4$ nanoparticle.

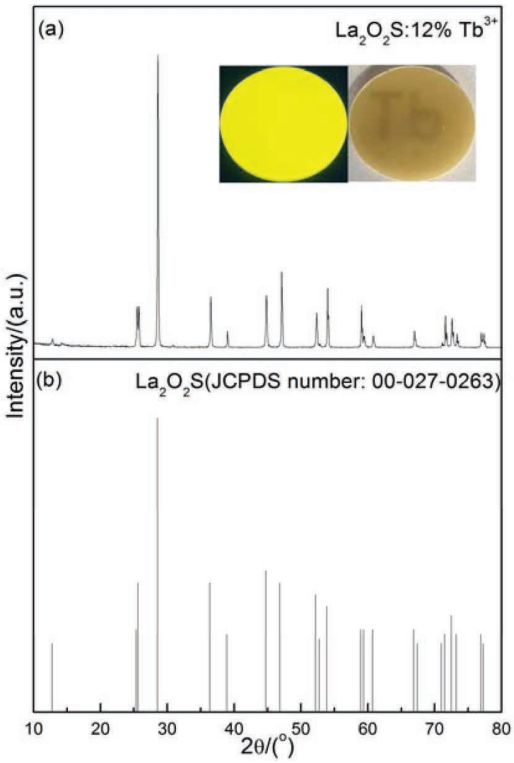

Fig. 8: (a) XRD pattern of La_2O_2S:12%Tb^{3+} phosphor and (b) standard diffraction peaks of La_2O_2S (JCPDS No. 00 – 027 – 0263), the inset of Fig. 8 shows photographs of the La_2O_2S:12%Tb^{3+} ceramic scintillator.

(3) Scintillation properties of $La_2O_2S:Tb^{3+}$ ceramic scintillator

Based on the analysis of luminescent results of $La_2O_2SO_4$:*x*%Tb^{3+} phosphors, we chose x = 12 % as the Tb^{3+} ions optimum doping concentration to prepare La_2O_2S:12%Tb^{3+} ceramic scintillator. Fig. 8 shows the XRD pattern of La_2O_2S:12%Tb^{3+} ceramic scintillator fabricated by sintering $La_2O_2SO_4$:12%Tb^{3+} phosphor in a hydrogen atmosphere. It shows that the phase of the sintered sample in Fig. 8(a) is well indexed to hexagonal phase of pure La_2O_2S (JCPDS card 00 – 027 – 0263), indicating $La_2O_2SO_4$:12%Tb^{3+} phosphor has completely converted into La_2O_2S:12%Tb^{3+} ceramic scintillator and the doped Tb^{3+} ions have no obvious impact on crystal structure composition. In addition, the inset of Fig. 8 shows that the La_2O_2S:12%Tb^{3+} ceramic scintillator appears greenish-yellow under 254 nm UV light irradiation with good translucency.

For further investigation of the scintillation properties, photographs of $CdWO_4$ single crystal and La_2O_2S:12%Tb^{3+} ceramic scintillator, x-ray images and light output curve comparisons between La_2O_2S:12%Tb^{3+} ceramic scintillator and $CdWO_4$ single crystal are shown in Fig. 9. The curve indicates that the light yield of the ceramic scintillator is around one third of that of the $CdWO_4$ single crystal.

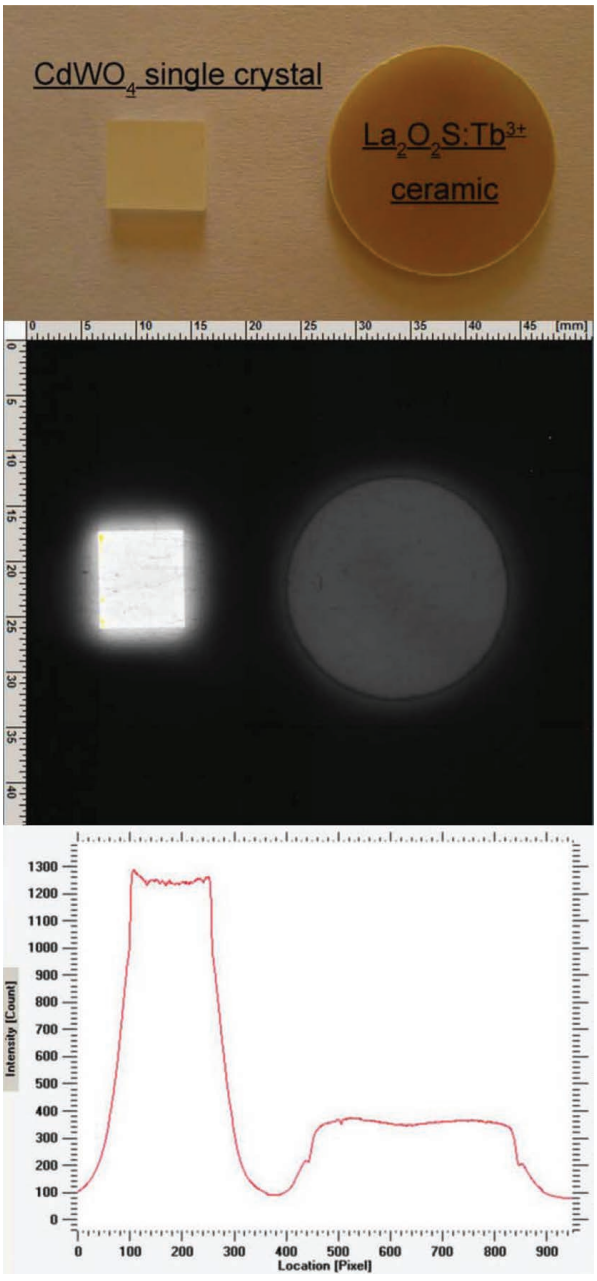

Fig. 9: Photographs of $CdWO_4$ single crystal and La_2O_2S:12%Tb^{3+} ceramic scintillator, X-ray image and light output curve comparison between $CdWO_4$ (left) and the La_2O_2S:12%Tb^{3+} ceramic scintillator (right).

As we know, afterglow value is an important evaluation standard in imaging, significantly affecting the speed

and repeatability of acquiring image data [32]. Fig. 10 shows the decay curve of $La_2O_2S:Tb^{3+}$ ceramic scintillator excited by X-rays. It shows when the luminescent intensity decreased to 1.03 % and 0.49 %, the decay times of the $La_2O_2S:Tb^{3+}$ ceramic scintillator reached 30 ms and 100 ms, respectively. It is worth noting that the light-out capability plays an important role in imaging system and detection performance. In addition, X-ray stopping power as well as the radiation damage value of ceramic scintillators also affect the scintillation properties [33]. Therefore, it is necessary to further systematically investigate and optimize the performance of $La_2O_2S:x\%Tb^{3+}$ ceramic scintillator.

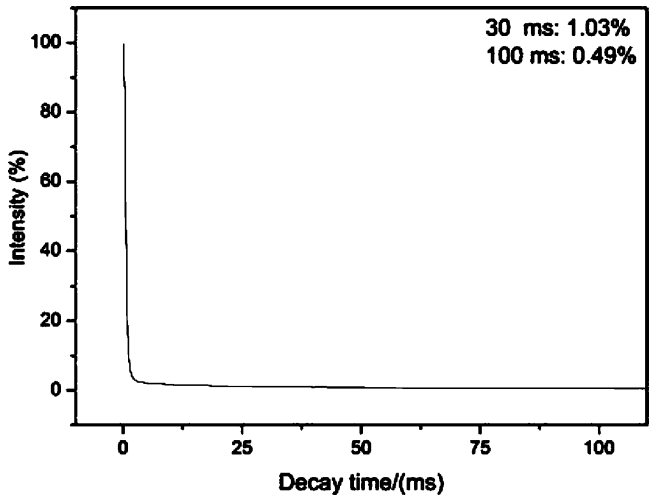

Fig. 10: Decay curve of 12%Tb^{3+}-ions-doped La_2O_2S ceramic scintillator.

IV. Conclusions

The $La_2O_2S:Tb^{3+}$ ceramic scintillator has been successfully synthesized with a simple co-precipitation method combined with pressureless reaction sintering in hydrogen. The XRD pattern shows that after calcination at 800 °C for 2 h, the precursor had completely transformed into pure $La_2O_2SO_4$ with tetragonal phase. Based on the analysis of photoluminescence, both the Tb^{3+}-ions-doped precursor and the $La_2O_2SO_4:Tb^{3+}$ phosphor possess green-light-emitting ability. But in comparison, $La_2O_2SO_4:Tb^{3+}$ phosphor possesses stronger excitation and emission peaks. Besides, under 374 nm UV light excitation, the strongest green emission peak at around 542 nm can be observed for $La_2O_2SO_4:Tb^{3+}$ phosphor. After being sintered in hydrogen atmosphere, $La_2O_2SO_4:Tb^{3+}$ phosphor has totally converted into $La_2O_2S:Tb^{3+}$ ceramic scintillator, appearing greenish-yellow with good translucency and a light output of around one third that of $CdWO_4$ single crystal, indicating that the pressureless reaction sintering method is an effective way to prepare $La_2O_2S:Tb^{3+}$ ceramic scintillator.

Acknowledgements

This work was supported by the National Students' Platform for Innovation and Entrepreneurship Training Program (No. 201710148000031), Nature Science Foundation of Liaoning Province of China (No. 20170540582) and the National Natural Science Foundation of China (No. 51701090).

References

1 Manigandan, R., Giribabu, K., Suresh, R., Munusamy, S., Praveen kumar, S., Muthamizh, S., Dhanasekaran, T., Padmanaban, A., Narayanan, V.: Synthesis, growth and photoluminescence behaviour of $Gd_2O_2SO_4:Eu^{3+}$ nanophosphors: The effect of temperature on the structural, morphological and optical properties, *RSC. Adv.*, **5**, 7515 – 7521, (2015).

2 Li, J.G., Wang, X.J., Liu, W.G., Zhu, Q., Li, X.D., Sun, X.D.: $(La_{0.97}RE_{0.01}Yb_{0.02})_2O_2S$ nanophosphors converted from layered hydroxyl sulfate and investigation of upconversion photoluminescence (RE=Ho, Er), *Nanoscale Res. Lett.*, **12**, 508, (2017).

3 Xie, M.B., Zhu, G.X., Li, D.Y., Pan, R.K., Fu, X.H.: $Eu^{2+}/Tb^{3+}/Eu^{3+}$ energy transfer in $Ca_6La_2Na_2(PO_4)_6F_2$:Eu, Tb phosphors, *RSC Adv.*, **6**, 33990 – 33997, (2016).

4 Koichi, K., Shiori, Y., Ken, K., Kiyoshi, K.: Highly transparent, bright green, sol-gel-derived monolithic silica-(Tb,Ce)PO_4 glass-ceramic phosphors, *RSC Adv.*, **4**, 26692 – 26696, (2014).

5 Li, H.D., Li, Y.J., Gu, S.N., Wang, F.Z., Zhou, H.L., Liu, X.T., Ren, C.J.: Enhancement of photocatalytic activity in Tb/Eu co-doped Bi_2MoO_6: the synergistic effect of Tb-Eu redox cycles, *RSC Adv.*, **6**, 48089 – 48098, (2016).

6 Xiao, Y., George, R.F., Robert, W., Jack, S.: Contrasting behaviour of the co-activators in the luminescence spectra of $Y_2O_2S:Tb^{3+}$, Er^{3+} nanometre sized particles under UV and red light excitation, *Nanoscale*, **5**, 1091 – 1096, (2013).

7 Benjamin, V., Jörg, N., Andreas, U., Rajesh, K., Markus, H.: Effect of the crystal structure of small precursor particles on the growth of β-$NaREF_4$ (RE = Sm, Eu, Gd, Tb) nanocrystals, *Nanoscale*, **5**, 806 – 812, (2013).

8 Kim, J., Piao, Y., Hyeon, T.: Multifunctional nanostructured materials for multimodal imaging, and simultaneous imaging and therapy, *Chem. Soc. Rev.*, **38**, 372 – 390, (2009).

9 Song, L.X., Du, P.F., Jiang, Q.X., Cao, H.B., Xiong, J.: Hydrothermal synthesis and photoluminescence properties of $Gd_2O_2SO_4:Eu^{3+}$ spherical phosphors, *J. Lumin.*, **150**, 50 – 54, (2014).

10 Wang, X., Liu, Q., Bu, Y., Liu, C.S., Liu, T., Yan, X.: Optical temperature sensing of rare-earth ion doped phosphors, *RSC Adv.*, **5**, 86219 – 86236, (2015).

11 Dong, H., Sun, L.D., Yan, C.H.: Energy transfer in lanthanide upconversion studies for extended optical applications, *Chem. Soc. Rev.*, **44**, 1608 – 1634, (2015).

12 Huang, X.Z., Liu, Z., Yang, Y.Y., Tian, Y.: Molten salt synthesis of $La_2O_2SO_4$ nanosheet and their luminescent properties with Eu^{3+} doping, *Funct. Mater. Lett.*, **6**, 1350019 – 1350012, (2013).

13 Luiz, C.M., Marcos, T.D.A., Hamilton, P.S.C., Jivaldo, R.M., Tlo, O.M.: Formation of oxysulfide LnO_2S_2 and oxysulfate $Ln_2O_2SO_4$ phases in the thermal decomposition process of lanthanide sulfonates (Ln= La, Sm), *J. Therm. Anal. Calorim.*, **107**, 305 – 311, (2012).

14 Tsuyoshi, K., Takeshi, I., Masami, S., Masafumi, U., Go, S.E.: Emission properties of Tb^{3+} in $Y_2O_2SO_4$ derived from their precursory dodecylsulfate-templated concentric- and straight-layered nanostructures, *J. Alloy. Compd.*, **485**, 730 – 733, (2009).

15 Machida, M., Kawamura, K., Kawano, T., Zhang, D., Ikeue, K.: Layered Pr-dodecyl sulfate mesophases as precursors of $Pr_2O_2SO_4$ having a large oxygen-storage capacity, *J. Mater. Chem.*, **16**, 3084 – 3090, (2006).

16 Wang, X.J., Li, J.G., Zhu, Q., Sun, X.D., Photoluminescence of $(La,Eu)_2O_2SO_4$ red-emitting phosphors derived from layered hydroxide, *J. Alloy. Compd.*, **5**, 28 – 34, (2014).

17 Lian, J.B., Sun, X.D., Liu, Z.G., Yu, J.Y., Li, X.D.: Synthesis and optical properties of $(Gd_{1-x}, Eu_x)_2O_2SO_4$ nano-phosphors by a novel co-precipitation method, *Mater. Res. Bull.*, **44**, 1822 – 1827, (2009).

18 Wang, X.J., Li, J.G., Molokeev, M.S., Zhu, Q., Li, X.D., Sun, X.D., Layered hydroxyl sulfate: controlled crystallization, structure analysis, and green derivation of multi-color luminescent (La, $RE)_2O_2SO_4$ and (La, $RE)_2O_2S$ phosphors (RE=Pr, Sm, Eu, Tb, and Dy), Chem. Eng. J., 15, 577 – 586, (2016).

19 Wang, X.J., Li, J.G., Maxim S.M., Wang, X.J., Liu, W.G., Zhu, Q., Hidehiko, T., Keiko, S., Byung, N.K., Yoshio, S.: Hydrothermal crystallization of a $Ln_2(OH)_4SO_4{\cdot}nH_2O$ layered compound for a wide range of ln (Ln=La-Dy), thermolysis, and facile transformation into oxysulfate and oxysulfide phosphors, *RSC. Adv.*, **7**, 13331 – 13339, (2017).

20 Wang, Y., Yang, B., Chen, X.M., Ma, W.H., Xu, B.Q.: Color-tunable and upconversion luminescence of Gd_2O_2S:Er, Tb phosphor, *Mater. Chem. Phys.*, **169**, 113 – 119, (2016).

21 Ding, Y.J., Zhang, Z.Y., Wang, L.X., Zhang, Q.T., Pan, S.B.: The role of sodium compound fluxes used to synthesize $Gd_2O_2S:Tb^{3+}$ by sulfide fusion method, *J. Mater. Sci.*, **28**, 2723 – 2730, (2016).

22 Jiang, G.C., Wei, X.T., Chen, Y.H., Duan, C.K., Yin, M., Yang, B., Cao, W.W.: Luminescent $La_2O_2S:Eu^{3+}$ nanoparticles as non-contact optical temperature sensor in physiological temperature range, *Mater. Lett.*, **143**, 98 – 100, (2015).

23 Yu, L.X., Li, F.H., Liu, H.: Fabrication and photoluminescent characteristics of one-dimensional $La_2O_2S:Eu^{3+}$ nanocrystals, *J. Rare. Earth.*, **31**, 356 – 359, (2013).

24 Wang, X.J., Zhu, Q., Li, J.G., Hu, Z.P., Zhu, G., Wang, C.: La_2O_2S:Tm/Yb as a novel phosphor for highly pure near-infrared upconversion luminescence, *Scripta Mater.*, **149**, 121 – 124, (2018).

25 Struebing, C., Lee, G., Wagner, B., Kang, Z.T.: Synthesis and luminescence properties of tb doped $LaBGeO_5$ and $GdBGeO_5$ glass scintillators, *J. Alloy. Compd.*, **686**, 9 – 14, (2016).

26 Greskovich, C., Duclos, S.: Ceramic scintillators, *Annu. Rev. Mater. Sci*., **27**, 69 – 88, (1997).

27 Bo, K.C., Jong, Y.K., Tae, J.K., Cheulmuu, S., Gyuseong, C.: Fabrication and imaging characterization of high sensitive CsI(Tl) and Gd_2O_2S(Tb) scintillator screens for X-ray imaging detectors, *Radiat. Meas.*, **45**, 742 – 745, (2010).

28 Orlovskii, Y.V., Basiev, T.T., Pukhov, K.K., Polyachenkova, M.V., Fedorov, P.P., Alimov, O.K., Gorokhova, E.I., Demidenko, V.A., Khristich, O.A., Zakalyukin, R.M.: Oxysulfide optical ceramics doped by Nd^{3+} for one micron lasing, *J. Lumin.*, **125**, 201 – 215, (2007).

29 Flores-Gonzalez, M.A., Ledoux, G., Roux, S., Lebbou, K., Perriat, P., Tillement, O.: Preparing nanometer scaled Tb-doped Y_2O_3 luminescent powders by the polyol method, *J. Solid State Chem.*, **178**, 989 – 997, (2005).

30 Dolo, J.J., Ntwaeaborwa, O.M., Terblans, J.J., Coetsee, E., Dejene, B.F., Biggs, M.M., Swart, H.C.: The effect of oxygen pressure on the structure, morphology and photoluminescence intensity of pulsed laser deposited $Gd_2O_2S:Tb^{3+}$ thin film phosphor, *Appl. Phys. A.*, **101**, 655 – 659, (2010).

31 Dai, Q.L., Song, H.W., Wang, M.Y., Bai, X., Dong, B., Qin, R.F., Qu, X.S., Zhang, H.: Size and concentration effects on the photoluminescence of $La_2O_2S:Eu^{3+}$ nanocrystals, *J. Phys. Chem. C*, **112**, 19399 – 19404, (2008).

32 Wang, W., Li, Y.S.: Fabrication of Gd_2O_2S:Pr, Ce, F scintillation ceramics by pressureless sintering in nitrogen atmosphere, *Int. J. Appl. Ceram. Technol*., **12**, 1 – 7, (2015).

33 Steven, J., Duclosa, C., Greskovicha, D.: Development of highlight TM scintillator for computed tomography medical imaging, *Nucl. Instrum. Meth. A*, **505**, 68 – 71, (2003).